

A MAGELLAN M2FS SPECTROSCOPIC SURVEY OF GALAXIES AT $5.5 < Z < 6.8$: PROGRAM OVERVIEW AND A SAMPLE OF THE BRIGHTEST $\text{Ly}\alpha$ EMITTERS

LINHUA JIANG¹, YUE SHEN^{2,3,16}, FUYAN BIAN^{4,17}, ZHEN-YA ZHENG^{5,6,7}, JIN WU^{1,8}, GRECCO A. OYARZÚN^{9,10}, GUILLERMO A. BLANC^{9,11}, XIAOHUI FAN¹², LUIS C. HO^{1,8}, LEOPOLDO INFANTE⁶, RAN WANG¹, XUE-BING WU^{1,8}, MARIO MATEO¹³, JOHN I. BAILEY, III^{13,14}, JEFFREY D. CRANE¹¹, EDWARD W. OLSZEWSKI¹², STEPHEN SHECTMAN¹¹, IAN THOMPSON¹¹, AND MATTHEW G. WALKER¹⁵

¹Kavli Institute for Astronomy and Astrophysics, Peking University, Beijing 100871, China; jiangKIAA@pku.edu.cn

²Department of Astronomy, University of Illinois at Urbana-Champaign, Urbana, IL 61801, USA

³National Center for Supercomputing Applications, University of Illinois at Urbana-Champaign, Urbana, IL 61801, USA

⁴Research School of Astronomy and Astrophysics, Australian National University, Weston Creek, ACT 2611, Australia

⁵CAS Key Laboratory for Research in Galaxies and Cosmology, Shanghai Astronomical Observatory, Shanghai 200030, China

⁶Institute of Astrophysics and Center for Astroengineering, Pontificia Universidad Catolica de Chile, Santiago 7820436, Chile

⁷Chinese Academy of Sciences South America Center for Astronomy, Santiago 7591245, Chile

⁸Department of Astronomy, School of Physics, Peking University, Beijing 100871, China

⁹Departamento de Astronomía, Universidad de Chile, Camino del Observatorio 1515, Las Condes, Santiago 7591245, Chile

¹⁰Department of Astronomy & Astrophysics, University of California, Santa Cruz, CA 95064, USA

¹¹Observatories of the Carnegie Institution for Science, 813 Santa Barbara Street, Pasadena, CA 91101, USA

¹²Steward Observatory, University of Arizona, 933 North Cherry Avenue, Tucson, AZ 85721, USA

¹³Department of Astronomy, University of Michigan, Ann Arbor, MI 48109, USA

¹⁴Leiden Observatory, Leiden University, P.O. Box 9513, 2300RA Leiden, The Netherlands

¹⁵McWilliams Center for Cosmology, Department of Physics, Carnegie Mellon University, Pittsburgh, Pennsylvania 15213, USA

¹⁶Alfred P. Sloan Research Fellow

¹⁷Stromlo Fellow

ABSTRACT

We present a spectroscopic survey of high-redshift, luminous galaxies over four square degrees on the sky, aiming to build a large and homogeneous sample of $\text{Ly}\alpha$ emitters (LAEs) at $z \approx 5.7$ and 6.5 , and Lyman-break galaxies (LBGs) at $5.5 < z < 6.8$. The fields that we choose to observe are well-studied, such as SXDS and COSMOS. They have deep optical imaging data in a series of broad and narrow bands, allowing efficient selection of galaxy candidates. Spectroscopic observations are being carried out using the multi-object spectrograph M2FS on the Magellan Clay telescope. M2FS is efficient to identify high-redshift galaxies, owing to its 256 optical fibers deployed over a circular field-of-view $30'$ in diameter. We have observed ~ 2.5 square degrees. When the program is completed, we expect to identify more than 400 bright LAEs at $z \approx 5.7$ and 6.5 , and a substantial number of LBGs at $z \geq 6$. This unique sample will be used to study a variety of galaxy properties and to search for large protoclusters. Furthermore, the statistical properties of these galaxies will be used to probe cosmic reionization. We describe the motivation, program design, target selection, and M2FS observations. We also outline our science goals, and present a sample of the brightest LAEs at $z \approx 5.7$ and 6.5 . This sample contains 32 LAEs with $\text{Ly}\alpha$ luminosities higher than $10^{43} \text{ erg s}^{-1}$. A few of them reach $\geq 3 \times 10^{43} \text{ erg s}^{-1}$, comparable to the two most luminous LAEs known at $z \geq 6$, ‘CR7’ and ‘COLA1’. These LAEs provide ideal targets to study extreme galaxies in the distant universe.

Keywords: cosmology: observations — galaxies: high-redshift — galaxies: formation — galaxies: evolution

1. INTRODUCTION

The epoch of cosmic reionization marks one of the major phase transitions of the universe, during which the neutral intergalactic medium (IGM) was ionized by the

emergence of early astrophysical objects. After that, the universe became highly structured and transparent to UV photons. Measurements of CMB polarization have determined the reionization peak at $z \sim 8.5$

(Planck Collaboration et al. 2016), and studies of high-redshift quasar spectra have located the end of reionization at $z \approx 6$ (Fan et al. 2006). High-redshift ($z \geq 6$) galaxies are a natural tool to probe the history of cosmic reionization, as well as the formation and evolution of early galaxies. Individual galaxies are usually too faint to provide useful information about the IGM state during the reionization era. However, such information can be drawn from their statistical properties, such as the evolution of the Ly α luminosity function. For example, recent studies have claimed that the Ly α luminosity function of Ly α emitters (LAEs) evolves rapidly from $z \sim 5.7$ to 6.5 (e.g., Kashikawa et al. 2006, 2011; Ouchi et al. 2008; Hu et al. 2010). This can be explained by the increasing neutral fraction of the IGM that attenuated Ly α emission via the resonant scattering of Ly α photons, and thus suggests the end of cosmic reionization at $z \sim 6$.

In recent years, with the advances of instrumentation on the *Hubble Space Telescope* (*HST*) and large ground-based telescopes such as the Subaru Telescope, the number of known high-redshift galaxies has increased dramatically. These galaxies can play an important role in studies of cosmic reionization (e.g., Silva et al. 2013; Treu et al. 2013; Cai et al. 2014; Dijkstra 2014; Jensen et al. 2014; Pentericci et al. 2016; Kakiichi et al. 2016; Ota et al. 2017; Zheng et al. 2017). The majority of the currently known galaxies at $z \geq 6$ are photometrically selected Lyman-break galaxies (LBGs) or candidates using the dropout technique. While large-area ground-based observations are efficient to select bright LBGs (e.g., Bowler et al. 2012; Curtis-Lake et al. 2012; Willott et al. 2013; Ono et al. 2017), faint LBGs were mostly found by *HST* (e.g., Yan et al. 2012; Ellis et al. 2013; Bouwens et al. 2015; Infante et al. 2015; Zitrin et al. 2015; Schmidt et al. 2016; Tilvi et al. 2016), with a substantial number of them at $z > 8$ (e.g., Laporte et al. 2012, 2015; Coe et al. 2013; Bouwens et al. 2014b; Oesch et al. 2014; McLeod et al. 2016). In addition, a small fraction of these LBGs, among the brightest in terms of the rest-frame UV luminosity, have been spectroscopically confirmed (e.g., Jiang et al. 2011; Toshikawa et al. 2012; Finkelstein et al. 2013; Oesch et al. 2015; Watson et al. 2015; Roberts-Borsani et al. 2016; Song et al. 2016). The latest development is the discovery of the galaxy GN-z11 at $z \sim 11$ from *HST* grism observations (Oesch et al. 2016).

The narrow-band (or Ly α) technique offers a complementary way to find high-redshift galaxies. Indeed, the first $z > 6$ galaxies were discovered to be LAEs at $z \simeq 6.5$ using the narrow-band technique (Hu et al. 2002; Kodaira et al. 2003; Rhoads et al. 2004). This technique can efficiently identify high-redshift galaxies

and has a high success rate of spectroscopic confirmation. Three dark atmospheric windows with little OH sky emission in the optical are often used to detect galaxies at $z \simeq 5.7$, 6.5, and 6.9. More than 200 LAEs have been spectroscopically confirmed at these redshifts (e.g., Taniguchi et al. 2005; Iye et al. 2006; Kashikawa et al. 2006, 2011; Shimasaku et al. 2006; Hu et al. 2010; Ouchi et al. 2010; Rhoads et al. 2012; Zheng et al. 2017). The narrow-band technique is also being used to search for higher redshift LAEs at $z > 7$ (e.g., Hibon et al. 2010; Tilvi et al. 2010; Krug et al. 2012; Ota & Iye 2012; Shibuya et al. 2012; Konno et al. 2014). All these Ly α surveys were made with ground-based instruments owing to their large fields-of-view (FoVs). In particular, the Subaru prime-focus imager Suprime-Cam (Miyazaki et al. 2002) has played a major role. Now, the new Subaru prime-focus imager Hyper Suprime-Cam (HSC) is being used to search for large samples of LAEs and LBGs at high redshift (e.g., Harikane et al. 2017; Konno et al. 2017; Ono et al. 2017; Ouchi et al. 2017; Shibuya et al. 2017).

Meanwhile, the physical properties of $z \geq 6$ galaxies are also being investigated. As the rest-frame UV and optical light from these galaxies moves to the infrared range, infrared observations using *HST* and the *Spitzer Space Telescope* (*Spitzer*) are critical for understanding these objects. Large samples are now being used to measure physical properties of high-redshift galaxies in a variety of aspects, such as UV slopes (e.g., Dunlop et al. 2012; Finkelstein et al. 2012; Bouwens et al. 2014a), galaxy morphology (e.g., Guaita et al. 2015; Kawamata et al. 2015; Shibuya et al. 2015, 2016; Curtis-Lake et al. 2016; Kobayashi et al. 2016; Liu et al. 2017), stellar populations and star formation rates (e.g., Egami et al. 2005; Stark et al. 2013; González et al. 2014; Faisst et al. 2016; Castellano et al. 2017; Karman et al. 2017). These studies are mostly based on photometrically selected samples; there are very few studies based on spectroscopically confirmed samples. Recently, Jiang et al. (2013a,b, 2016) carried out deep *HST* and *Spitzer* observations of a sample of 67 spectroscopically confirmed LAEs and LBGs at $5.7 < z < 7.0$, and conducted an extensive analysis of the physical properties of these galaxies. Yet the number of such studies is still very limited so far (e.g. Bowler et al. 2017a).

Despite the progress that has been made on studies of high-redshift galaxies, the number of spectroscopically confirmed galaxies is relatively small. For example, it has been found that the Ly α luminosity function evolves rapidly from $z \sim 5.7$ to 6.5, as mentioned earlier, but there are large discrepancies (a factor of $\sim 2 - 3$) among the normalizations of the luminosity functions in different studies (Kashikawa et al.

2006, 2011; Ouchi et al. 2008; Hu et al. 2010). In addition, there are also discrepancies between the results from spectroscopically confirmed samples and photometrically selected samples (e.g., Matthee et al. 2015; Santos et al. 2016; Bagley et al. 2017). The reasons for these discrepancies are still not clear, but cosmic variance, sample incompleteness, and target contamination are some of the main reasons. If so, a much larger LAE sample with high completeness and secure redshifts over a large area is the only solution. Furthermore, studies of physical properties of spectroscopically confirmed galaxies are limited. The current spectroscopically confirmed samples usually consists of several to a few tens of galaxies, which are much smaller than photometrically selected samples with hundreds of galaxies.

In this paper, we present a large spectroscopic survey of galaxies at $5.5 < z < 6.8$, using the large FoV, fiber-fed, multi-object spectrograph M2FS (Mateo et al. 2012) on the 6.5m Magellan Clay telescope. Taking advantage of a $30'$ -diameter FoV, M2FS is one of the most efficient instruments to identify relatively bright high-redshift galaxies (e.g., Oyarzún et al. 2016, 2017). The fields that we chose to observe are well-studied deep fields, including the Subaru XMM-Newton Deep Survey (SXDS), A370, the Extended Chandra Deep Field-South (ECDFS), COSMOS, and SSA22. They cover a total of $\sim 4 \text{ deg}^2$. We have observed about 2.5 deg^2 so far, and have discovered a giant protocluster at $z = 5.70$ (Jiang et al. 2017). Here we will provide an overview of the program, and show one of our first scientific results: a sample of the brightest LAEs at $z \approx 5.7$ and 6.5 . In this paper, we call galaxies found by the narrow-band technique LAEs, and those found by the dropout technique LBGs. This LAE/LBG classification only reflects the methodology that we apply to select galaxies (e.g., Jiang et al. 2013a,b, 2016). We do not discuss galaxies identified by blind searches (e.g., Dressler et al. 2011; Henry et al. 2012).

The layout of the paper is as follows. In Section 2, we introduce the deep fields that we chose to observe, the imaging data, and the target selection. In Section 3, we describe the M2FS observations and data reduction. In Section 4, we present our planned science cases, and then present a sample of very luminous LAEs. We summarize our paper in Section 5. Throughout the paper, all magnitudes are expressed on the AB system. We use a Λ -dominated flat cosmology with $H_0 = 68 \text{ km s}^{-1} \text{ Mpc}^{-1}$, $\Omega_m = 0.3$, and $\Omega_\Lambda = 0.7$.

2. SURVEY FIELDS AND IMAGING DATA

In this section, we describe the fields that we selected for our program and the imaging data that we used for our target selection. These fields are well-studied with a large number of existing data. In particular, the fields

were chosen to have deep Subaru Suprime-Cam imaging data in the optical, especially in two narrow-band (NB) filters, NB816 and NB921 (and/or NB912), which correspond to the detection of LAEs at $z \simeq 5.7$ and 6.5 . The full widths at half maximum (FWHM) of the two filters are roughly 120 and 132 Å. The Suprime-Cam is a wide-field prime-focus imager for the 8.2m Subaru telescope. With a FoV of $34' \times 27'$, it has played a major role in finding LAEs at $z \geq 5.7$.

Our fields are summarized in Table 1. Column 2 gives the field names. Column 3 shows the central coordinates of the fields. Column 4 is the area coverage. Columns 5–8 list the magnitude limits of the NB816, NB921, NB912, and z -band images that were used to select our galaxy candidates. The details of the individual fields are explained in the following subsections. As we will see, some areas have been covered by previous spectroscopic observations. We include them to cross check our target contamination and sample completeness.

2.1. Imaging Data

We briefly describe the imaging data used for our target selection below. Our fields generally have very deep images in a series of broad and narrow bands in the optical. As we mentioned above, the images were taken with Subaru Suprime-Cam, and were retrieved from the archival server SMOKA (Baba et al. 2002). The images were reduced, re-sampled, and co-added using a combination of the Suprime-Cam Deep Field REDuction package (Yagi et al. 2002) and our own IDL routines. The details are given in Jiang et al. (2013a). The following is a brief summary.

Our data processing began with the raw images with point spread function (PSF) sizes better than $1''.2$. Each image was bias (overscan) corrected and flat-fielded. Bad pixel masks were created from flat-field images. Then cosmic rays, saturated pixels, and bleeding trails were identified and interpolated. For each image, a weight mask was generated to include these defective pixels. We then corrected the image distortion, subtracted the sky-background, and masked out the pixels affected by the Auto-Guider probe. After individual images were processed, we extracted sources with SExtractor (Bertin & Arnouts 1996), and used these sources to calculate astrometric and photometric solutions with SCAMP (Bertin 2006). Both science and weight-map images were scaled and updated using the astrometric and photometric solutions measured above. We also incorporated PSF information into the weight image, i.e., weight is inversely proportional to the square of PSF. We re-sampled and co-added images using SWARP (Bertin et al. 2002). The re-sampling interpolations for science and weight images were LANCZOS3 and BILINEAR, respectively.

Table 1. Survey Fields

No.	Field	Coordinates (J2000.0)	Area (deg ²)	$m_{\text{lim}}(\text{NB816})$ (mag)	$m_{\text{lim}}(\text{NB912})$ (mag)	$m_{\text{lim}}(\text{NB921})$ (mag)	$m_{\text{lim}}(z')$ (mag)
(1)	(2)	(3)	(4)	(5)	(6)	(7)	(8)
1	SXDS	02:18:00–05:00:00	1.0	26.1	...	25.4	26.2
2	A370a	02:39:55–01:35:24	0.2	26.0	25.8	26.0	26.3
3	A370b	02:41:16–01:34:30	0.2	25.9	25.9	...	25.9
4	ECDFS	03:32:25–27:48:18	0.2	26.0	...	26.0	26.7
5	COSMOS	10:00:29+02:12:21	2.0	25.7	...	25.8	25.5
6	SSA22a	22:17:32+00:15:14	0.2	26.1	25.7	25.5	26.7
7	SSA22b	22:18:23+00:37:08	0.2	26.2	25.6	...	25.9

NOTE—The magnitude limits correspond to 5σ detections in a $2''$ diameter aperture.

We then ran `SExtractor` on the final co-added images to detect sources. We performed flux calibration for broad-band images using the results of [Yagi et al. \(2013\)](#). Flux calibration for narrow-band images was done using the colors between narrow bands and nearby broad bands for the Suprime-Cam system (e.g., [Taniguchi et al. 2005](#); [Shimasaku et al. 2006](#); [Ouchi et al. 2008](#)). We measured aperture photometry in a $2''$ diameter aperture. Then an aperture correction was applied to correct for light loss. The aperture correction is determined from a large number of bright, but unsaturated point sources in the same image.

2.2. Survey Fields

2.2.1. The SXDS field

The Subaru deep survey projects, including SXDS ([Furusawa et al. 2008](#)) and the Subaru Deep Field (SDF; [Kashikawa et al. 2004](#)), have been very successful in searching for $z \geq 6$ galaxies. SXDS consists of five Suprime-Cam pointings (Figure 1), and covers $\sim 1.2 \text{ deg}^2$ in total ([Furusawa et al. 2008](#)). It has one of the deepest optical imaging datasets among ground-based surveys. The imaging data in five broad bands $BVRiz'$ reach depths of 27.9, 27.6, 27.4, 27.4, and 26.2 AB mag (5σ in a $2''$ diameter aperture), respectively. Especially noteworthy is the availability of deep observations with a series of narrow-band filters, including NB816 and NB921. The depths of the stacked NB816 and NB921-band images are 26.1 and 25.4 mag, respectively. Note that the depths slightly vary (± 0.1 mag) across the five different Suprime-Cam pointings. In addition to the optical imaging data, the SXDS central region ($\sim 0.8 \text{ deg}^2$) is covered by deep near-IR imaging data from the UKIDSS Ultra Deep Survey (UDS). The UDS field has a series of deep imaging data from ultraviolet to radio. For exam-

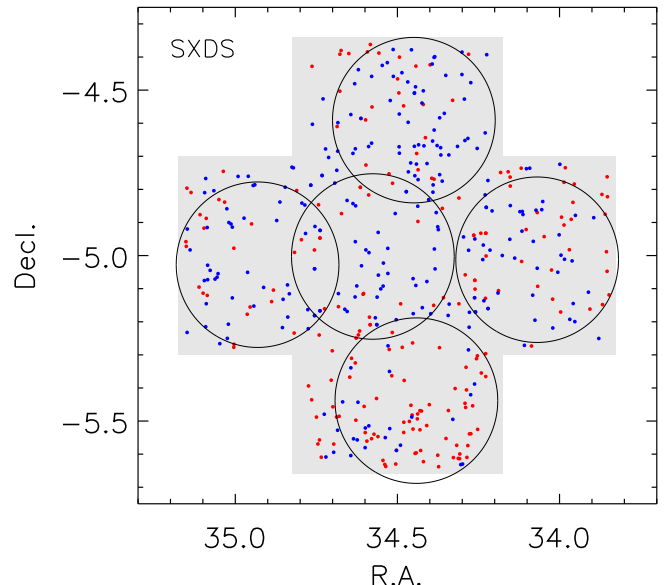


Figure 1. The SXDS field. The field consists of five Suprime-Cam pointings (grey area) and covers $\sim 1.2 \text{ deg}^2$ in total ([Furusawa et al. 2008](#)). The five large circles indicate the five M2FS pointings. The red and blue points represent LAE and LBG candidates, respectively.

ple, it is partly covered by the HST CANDELS survey ([Grogin et al. 2011](#); [Koekemoer et al. 2011](#)).

The SXDS images have been used to search for high-redshift LAEs, including $z \approx 5.7$ and 6.5 LAEs. [Ouchi et al. \(2008\)](#) presented a large sample of LAE candidates at $z \approx 3.1$, 3.7 , and 5.7 . They also reported on the spectroscopic confirmation of 17 $z \approx 5.7$ LAEs from a sample of 29 candidates. [Ouchi et al. \(2010\)](#) presented a photometric sample of LAE at $z \approx 6.5$. They also took spectroscopic observations of 30 candidates and identified 19 LAEs. [Matthee et al. \(2015\)](#) reported on a small sample of bright photometrically selection LAEs at

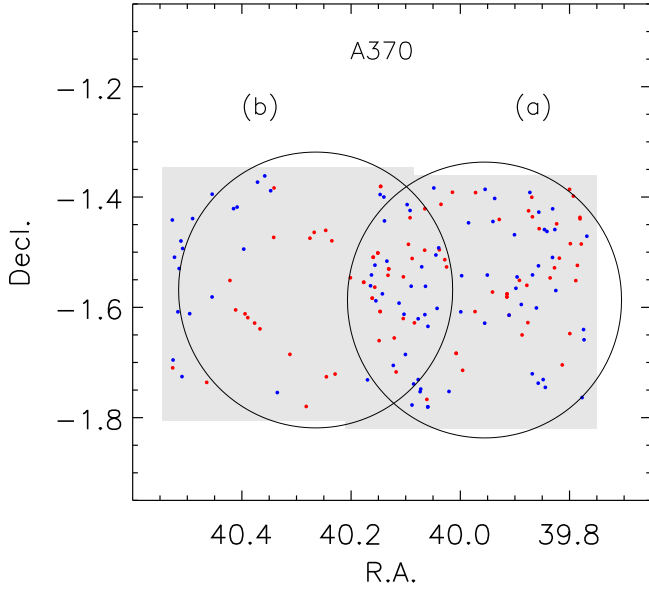


Figure 2. The A370 field. The field consists of two Suprime-Cam pointings (grey area), denoted as A370a and A370b in the paper. The two large circles indicate the two M2FS pointings. The red and blue points represent LAE and LBG candidates, respectively.

$z \approx 6.5$. In our program, we will observe most $z \approx 5.7$ and 6.5 LAE candidates brighter than 7σ detections, over the whole SXDS field.

2.2.2. The A370 field

The A370 field consists of two Suprime-Cam pointings, denoted as A370a and A370b in the paper (Figure 2). A370a is centered on the famous galaxy cluster Abell 370 at $z = 0.375$. The cluster is one of the best studied strong-lensing clusters, and the cluster region has a wealth of multi-wavelength data. It is one of the HST Frontier Fields (Lotz et al. 2017). The Suprime-Cam imaging data in five broad bands ($BVRiz'$) reach depths of 27.7, 27.0, 27.0, 26.2, and 26.3 mag, respectively. It is also covered in three narrow bands, NB816, NB912, and NB921, and the depths in these bands are 26.0, 25.8, and 26.0 mag, respectively.

A370b slightly overlaps with A370a. The Suprime-Cam imaging data in four broad bands ($BRIz'$) have depths of 27.3, 27.5, 26.4, and 26.1 mag, respectively. We also have a V -band image, but it is too shallow compared to other images, so we did not use it. This does not affect our target selection of high-redshift objects. The image depths in two narrow bands (NB816 and NB912) are 25.9 mag. We do not have NB921-band images for A370b.

Hu et al. (2010) has carried out deep spectroscopy of $z \approx 5.7$ and 6.5 LAE candidates in the A370 field, and confirmed 24 LAEs. They did not use the NB921-band image, and did not observe $z \geq 6$ LBG candidates. In our program, we use both NB912- and NB921-band im-

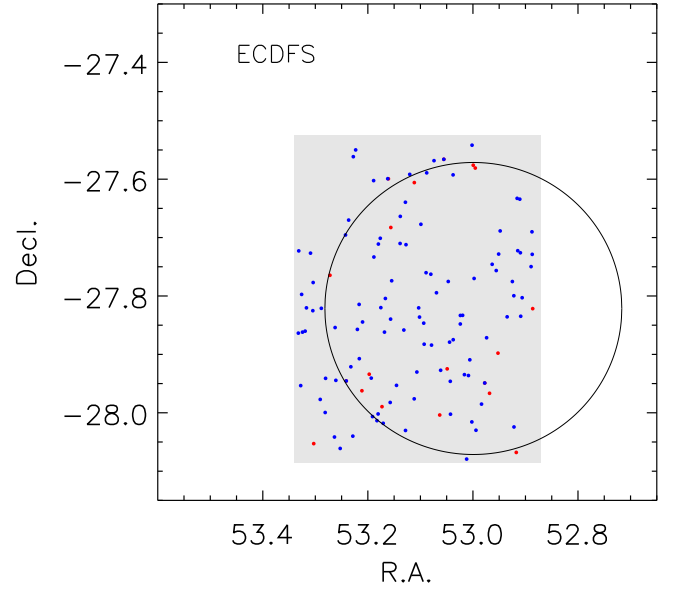


Figure 3. The ECDFS field. The field consists of one Suprime-Cam pointing (grey area). The large circle indicates the M2FS pointing. We have to move the pointing center far away from the field center to find a suitable SH star. The red and blue points represent LAE and LBG candidates, respectively.

ages for $z \approx 6.5$ LAEs, and we also target LBGs at $z \geq 6$.

2.2.3. The ECDFS field

The ECDFS field consists of one Suprime-Cam pointing (Figure 3). It is partly covered by deep X-ray data (e.g., Lehmer et al. 2005; Xue et al. 2016; Luo et al. 2017), as well as other multi-wavelength data. In particular, it is partly covered by several HST deep fields. It has deep Suprime-Cam r' and z' -band images with depths of 27.4 and 26.7 mag. The depths of its two narrow-band images in NB816 and NB921 are 26.0 mag. This field does not have Suprime-Cam i' or I -band images (the i' or I -band data are critical for target selection here). We have generated a pseudo i' -band image as follows. ECDFS was observed in a series of more than 15 narrow and intermediate bands by Suprime-Cam. We combined these images that have central wavelengths within the wavelength coverage of the Suprime-Cam i' filter. The photometric zero point of the stacked pseudo image was determined by comparing the $i' - z'$ colors of the objects in this image to those from other fields with i' and z' -band images. The depth of this pseudo i' -band image is 27.5 mag. The wavelength coverage of the pseudo i' band is slightly different from that of the Suprime-Cam i' filter. This has little effect on the selection of LAE candidates, but slightly affects the selection of LBG candidates (or i' -band dropouts) due to a small difference on the red-end wavelength cutoff. We take this into account for target selection.

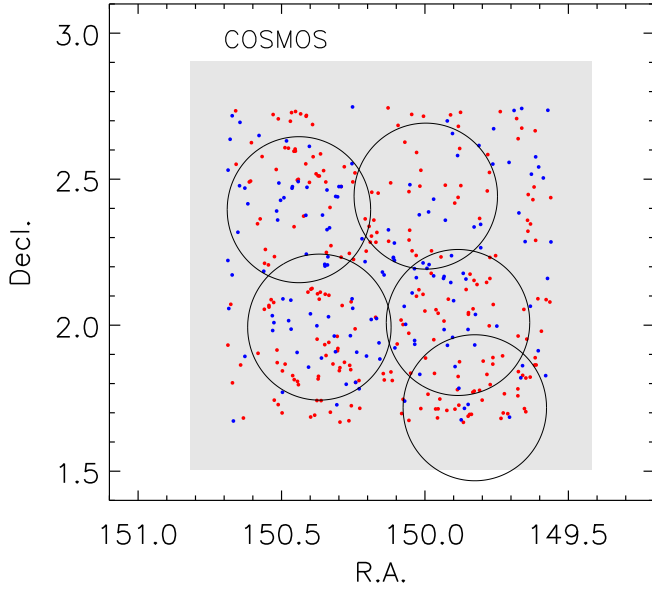


Figure 4. The COSMOS field. The field covers $\sim 2 \text{ deg}^2$ in total (grey area). So far we have only considered the central $\sim 1 \text{ deg}^2$ region that has the NB921-band imaging data. The five large circles indicate the five M2FS pointings. The red and blue points represent LAE and LBG candidates, respectively.

2.2.4. The COSMOS field

The COSMOS field (Scoville et al. 2007) covers $\sim 2 \text{ deg}^2$ (Figure 4) and has extensive multi-wavelength images (e.g., Capak et al. 2007). For example, it is partly covered by the UltraVISTA near-IR imaging data and the HST CANDELS data. Taniguchi et al. (2007) presented Suprime-Cam observations of COSMOS in detail. These observations cover the whole COSMOS field in six broad bands ($Bg'r'i'z'$) and one narrow band NB816. Capak et al. (2007) released the images to the public. These images were smoothed to a large PSF size ($\sim 1''6$) for better photometric redshift measurement. Our stacked images have better PSF sizes ($\sim 1''0 - 1''2$). In seven bands $BVr'i'z'$ and NB816, they have depths of 27.3, 26.7, 26.7, 26.3, 25.5, and 25.7 mag, respectively. We did not use the g' images because of their poor image quality. The central part of COSMOS (roughly 1 deg^2) was also observed in the NB921 band. The stacked NB921-band image that we produced has a depth of 25.8 mag.

Murayama et al. (2007) presented a sample of 119 LAE candidates at $z \approx 5.7$. They did not carry out spectroscopic observations of these candidates. Matthee et al. (2015) reported on a sample of bright photometrically selected LAEs at $z \approx 6.5$. In our program, we spectroscopically identify $z \approx 5.7$ and 6.5 LAE candidates, as well as LBG candidates. So far we have only considered the region covered by the NB921-band image. We will complete observations for the whole

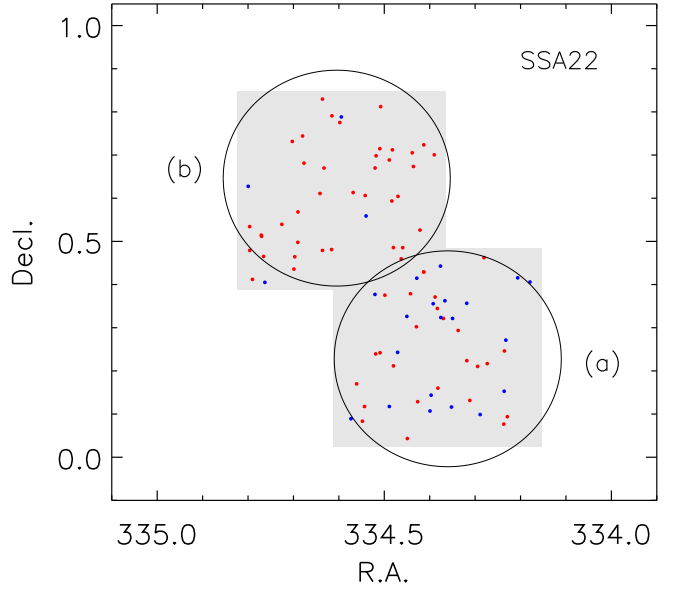


Figure 5. The SSA22 field. The field consists of two Suprime-Cam pointings (grey area), denoted as SSA22a and SSA22b in the paper. The two large circles indicate the two M2FS pointings. The red and blue points represent LAE and LBG candidates, respectively.

COSMOS field later.

2.2.5. The SSA22 field

The SSA22 field consists of two Suprime-Cam pointings, denoted as SSA22a and SSA22b in the paper (Figure 5). SSA22a and SSA22b slightly overlap with each other. For SSA22a, the Suprime-Cam imaging data in five broad bands ($BVRIz'$) reach depths of 27.9, 28.1, 28.0, 27.3, and 26.7 mag, respectively. It is also covered in three narrow bands, NB816, NB912, and NB921, and the depths in these bands are 26.1, 25.7, 25.5 mag, respectively. For SSA22b, the Suprime-Cam imaging data in the five broad bands reach depths of 27.6, 27.2, 27.2, 26.5, and 25.9 mag. Its two narrow-band images in NB816 and NB912 have depths of 26.2 and 25.6 mag.

Hu et al. (2010) has carried out deep spectroscopy of $z \approx 5.7$ and 6.5 LAE candidates in the SSA22 field, and confirmed nearly 50 LAEs. They did not use the NB921-band data, and did not observe LBG candidates. Matthee et al. (2015) reported a sample of bright, photometrically selected LAEs at $z \approx 6.5$. In our program, we use both NB912- and NB921-band images to select $z \approx 6.5$ LAEs. We also observe $z \geq 6$ LBG candidates.

3. TARGET SELECTION, M2FS OBSERVATIONS, AND DATA REDUCTION

In this section, we briefly describe our target selection of LAE and LBG candidates, and then present the details of the M2FS observations and data reduction. One advantage of M2FS is its large number (256) of fibers available. This allows us to relax target selection crite-

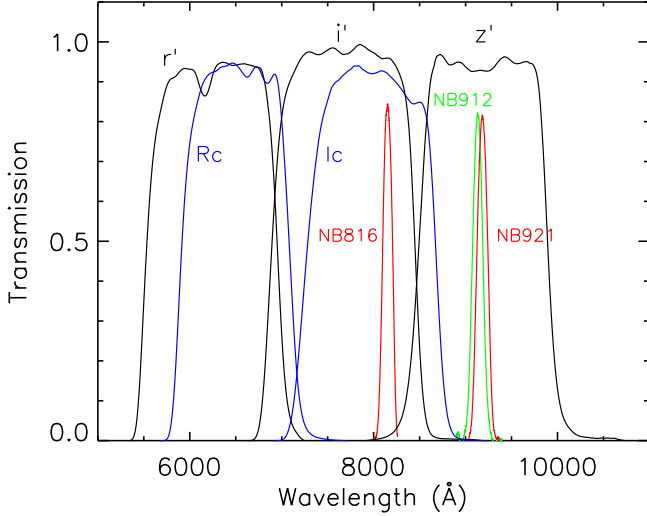


Figure 6. Transmission curves of the main Suprime-Cam filters that are used for our target selection. The NB816 and NB921 (or NB912) bands correspond to the detection of LAEs at $z \simeq 5.7$ and 6.5, respectively.

ria so that we can include more candidates and improve sample completeness.

3.1. Target Selection

We select LAE and LBG candidates using the narrow-band (or Ly α) technique and the dropout technique, respectively. The two techniques used for high-redshift galaxies have been extensively addressed in the literature. Figure 6 shows the filters that are used for our target selection. Different fields have slightly different combinations of broad-band filters¹, such as $r'i'z'$, $Ri'z'$, and RIz' . As an example, below we use $Ri'z'$ to briefly present our selection criteria for the SXDS field.

The selection of $z \approx 5.7$ LAE candidates is mainly based on the $i' - \text{NB816}$ color (top panel in Figure 7). We apply the following color cuts to all $> 7\sigma$ detections in the NB816 band,

$$\begin{aligned} i' - \text{NB816} &> 1.0, \\ R - z' &> 2 \text{ or } R < 3\sigma \text{ detection,} \end{aligned} \quad (1)$$

where the second criterion requires $R - z' > 2$ if a candidate is detected in z' ; otherwise, it requires that the R -band detection is fainter than 3σ . We further require that candidates should not be detected ($< 2\sigma$) in any bands bluer than R , assuming that no flux can be detected at the wavelength bluer than the Lyman limit. We visually inspect each candidate, and remove spurious detections.

The selection of $z \approx 6.5$ LAE candidates is mainly based on the $z' - \text{NB921}$ (or $z' - \text{NB912}$) color (middle

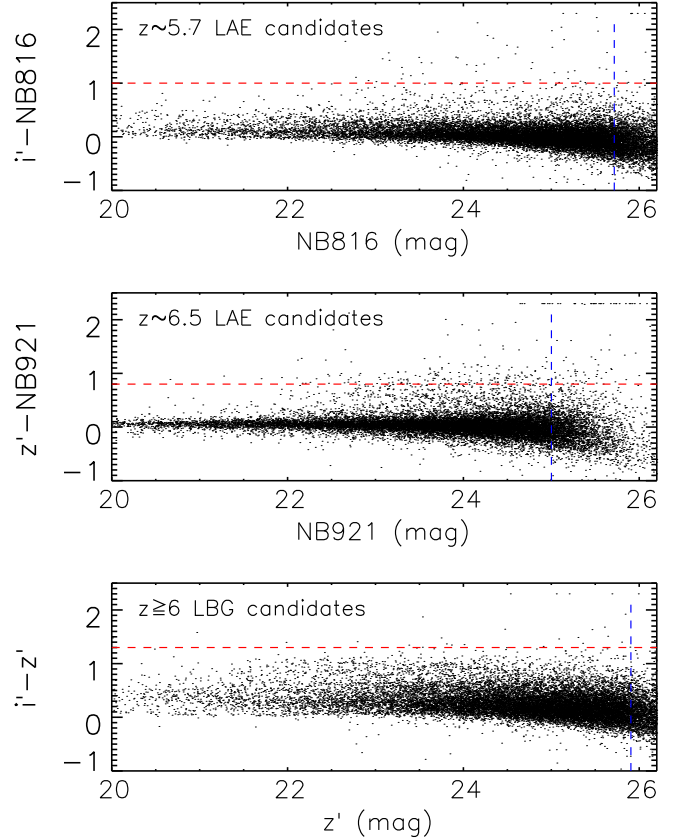


Figure 7. Color-magnitude diagrams that are used for our target selection of $z \approx 5.7$ and 6.5 LAE candidates, and $z \geq 6$ LBG candidates. Each panel contains roughly 20,000 objects selected from the SXDS catalog. Colors greater than 2.3 are shown as 2.3 in the figure. The red dashed lines indicate our color cuts and the blue dashed lines indicate the 7σ limits.

panel in Figure 7). We apply the following color cuts to all $> 7\sigma$ detections in the NB921 (or NB912) band,

$$\begin{aligned} z' - \text{NB921} &> 0.8, \\ i' - z' &> 1.3 \text{ or } i' < 3\sigma \text{ detection,} \\ R - z' &> 2.5 \text{ or } R < 3\sigma \text{ detection.} \end{aligned} \quad (2)$$

We also visually inspect each candidate, and require no detection ($< 2\sigma$) in any bands bluer than R .

The selection of $z \geq 6$ LBG candidates is mainly based on the $i' - z'$ color (bottom panel in Figure 7). The survey limit is also 7σ detections in the z' band. We apply the following color cuts,

$$\begin{aligned} i' - z' &> 1.3 \text{ or } i' < 3\sigma \text{ detection,} \\ R - z' &> 2.0 \text{ or } R < 3\sigma \text{ detection.} \end{aligned} \quad (3)$$

As for the LAE candidates, we require no detection ($< 2\sigma$) in any bands bluer than R . Each candidate is also visually inspected.

As we can see, our selection criteria are relatively conservative, compared to those used in the literature (e.g., Taniguchi et al. 2005; Shimasaku et al. 2006;

¹ In this paper, the Suprime-Cam filter Rc is denoted as R , and Ic is denoted as I .

Table 2. Numbers of Targets

Field No. ^a	Field Name	$z \sim 5.7$ LAEs	$z \sim 6.5$ LAEs	$z \sim 6$ LBGs	Other targets
(1)	(2)	(3)	(4)	(5)	(6)
1	SXDS	121/162	35/39	205/249	392
2,3	A370	21/22	61/63	74/85	91
4	ECDFS	3/3	9/12	71/105	159
5	COSMOS	18/21	160/226	105/145	828
6,7	SSA22	17/17	45/48	21/24	223

^aNumbers correspond to Column 1 in Table 1.

NOTE—In Columns 3–5, the latter number in each field indicates the total number of candidates, and the former number indicates the number of candidates that were observed (or will be observed) by our M2FS program. Column 6 shows the actual numbers of ancillary targets that were observed (or will be observed).

Ouchi et al. 2008, 2010; Hu et al. 2010). This allows us to include less promising candidates and achieve high completeness. On the other hand, it means a relatively lower efficiency (a larger fraction of contaminants). However, it is not a concern in our program, since we have enough fibers to cover all these candidates. Because of the same reason, we do not use near-IR imaging data for our target selection. As we mentioned earlier, some fields are covered by deep near-IR imaging data, which can potentially remove some contaminants. For example, many contaminants of high-redshift galaxies are late-type dwarf stars and low-redshift red (dusty) galaxies, which tend to have different (redder) colors in the (observed-frame) near-IR. For the purpose of sample completeness, we do not use these near-IR data. We choose to use simple color cuts in the optical to achieve high completeness.

In addition to the above main targets of $z \geq 6$ galaxies, we also select a variety of ancillary targets for spare fibers. First of all, we include some weak LAE and LBG candidates with detections lower than 7σ in the narrow bands or z' band. Our main targets have $> 7\sigma$ detections. As candidates go fainter, the contamination rate rises rapidly. Nevertheless, we include a sample of LAE and LBGs with detections between 5σ and 7σ , using the same selection criteria 1–3. We also include other ancillary targets. Here are three examples: 1) strong X-ray sources that have not been spectroscopically identified; 2) relatively lower-redshift LBG candidates at $5.3 < z < 5.5$; 3) z' -band dropout objects if y -band images are available. These targets do not form complete samples.

The selection criteria may slightly vary from field to field, depending on the bands of the available imaging data, image depth, and candidate surface density. All

targets are prioritized before they are fed to fiber plates. Candidate LAEs at $z \approx 6.5$ and 5.7 have the highest priorities, followed by i' -band dropout objects (LBG candidates), and finally ancillary targets. Table 2 shows the numbers of the targets selected earlier, and the numbers of the targets that have been observed (or will be observed) by our M2FS program. More detailed information will be presented in the future papers when we study galaxy properties and luminosity functions.

3.2. M2FS Observations

3.2.1. Plate design

M2FS, the Michigan/Magellan Fiber System, is a fiber-fed, multi-object, double optical spectrograph on the Magellan Clay telescope (Mateo et al. 2012). Each spectrograph is fed by 128 fibers, resulting in a total of 256 fibers. M2FS provides a large FoV of $30'$ in diameter. It has high throughput in the wavelength range from 3700 to 9500 Å. We use a pair of red-sensitive gratings with a resolving power of about 2000. The wavelength coverage of our observations is roughly from 7600 to 9600 Å, corresponding to the wavelength of Ly α emission in galaxies at $z \approx 5.3 - 6.8$.

The design of the M2FS pointings or plug plates is limited by the availability of Shack-Hartmann (SH) stars, guide stars, and alignment stars. Each plate (or M2FS field) is centered on a SH star, which is fed to SH wavefront sensors for primary-mirror wavefront corrections. The SH star is required to be brighter than $V = 14$ mag. At least two guide stars are needed for each plate, and they are brighter than $V = 15$ mag. In addition, each plate requires at least four (up to eight) alignment stars brighter than $V = 15.5$ mag. These restrictions have impact on our selection of M2FS pointing centers, due to the small numbers of bright stars in our fields. Note

Table 3. Summary of the M2FS Observations

Field No. ^a	Field Name	Year/Month	Exp. Time	Comments
(1)	(2)	(3)	(4)	(5)
1	SXDS1	2016 November, December	5.0 hrs	20% data not usable
1	SXDS2	2016 December	5.0 hrs	
1	SXDS3	2015 November	7.0 hrs	
1	SXDS5	2016 December	5.0 hrs	
2	A370a	2015 September, November	7.0 hrs	cloudy (3 hrs), cirrus (4 hrs)
4	ECDFS	2016 February	6.3 hrs	
5	COSMOS1	2015 April	6.0 hrs	cirrus (2 hrs)
5	COSMOS2	2015 April	4.5 hrs	
5	COSMOS3	2015 April	5.0 hrs	
5	COSMOS4	2015 April	5.0 hrs	
5	COSMOS5	2016 February	5.7 hrs	
7	SSA22b	2015 September	7.5 hrs	cirrus (4 hrs)

^aField numbers correspond to Column 1 in Table 1.

that these fields were chosen to have few bright stars in the first place. An extreme sample is the ECDFS field (see Figure 3), where several HST deep fields are located. We had to shift the M2FS pointing center far away from the field center to find a suitable SH star.

In addition to the science targets and bright setup stars, we also include 5–10 relatively bright point sources in each field. They are used as reference stars to check image quality and depth.

Finally, we include sky fibers. The number of sky fibers varies around 30–40, depending on the availability of spare fibers. Sky fibers are critical for sky subtraction, and more sky fibers usually lead to better sky subtraction. On the other hand, our main targets are very faint high-redshift galaxy candidates, and they are mostly much fainter than sky background. So most fibers for the galaxy candidates can be used as sky fibers. As a result, roughly half of the total fibers can be used as sky fibers, which allows us to achieve accurate sky subtraction (see the next subsection for details).

3.2.2. Observations

Our goal is to detect $z \approx 5.7$ LAEs down to at least 25.5–25.6 mag in the NB816 band. This corresponds to a Ly α flux depth of $\sim 1 \times 10^{-17}$ erg s $^{-1}$ cm $^{-2}$ ($> 5\sigma$ detection). The total integration time per pointing was initially set to be 5 hours, based on the theoretical system throughput. Later we found that we were able to achieve our goal with this integration under normal weather conditions. Accordingly, we are able to detect $z \approx 6.5$ LAEs down to at least 25.2 mag (in the NB921

or NB912 band).

Table 3 summarizes the M2FS observations that we have carried out so far. The five SXDS M2FS pointings are denoted as SXDS1, SXDS2, SXDS3, SXDS4, and SXDS5, and the five COSMOS pointings are denoted as COSMOS1, COSMOS2, COSMOS3, COSMOS4, and COSMOS5. We have observed most fields or pointings. The remaining pointings will be observed in the near future.

The M2FS observations are made in queue mode, and the M2FS observing blocks are typically scheduled in dark or gray time. The observing conditions for our fields were usually normal, with relatively clear skies and $\sim 0''.7 - 1''.0$ seeing. A small fraction of images were collected in relatively poor conditions (see Table 3). The on-source integration time for each pointing was about 5–6 hours, consisting of several individual exposures. The individual exposure time was typically 1 hr, and can be 30 min or 45 min, depending on weather condition and airmass. In addition to science images, we also took a set of calibration images in the afternoon or during the night. The calibration data include bias, twilight flats, dark, lamps, fiber maps, etc. All images were binned with two by two pixels.

3.3. Data Reduction

The data reduction of our M2FS images is not straightforward, due to the following reasons. First of all, the wavelength range considered here is contaminated by a large number of strong OH skylines. The spectral resolution is not optimal for efficiently remov-

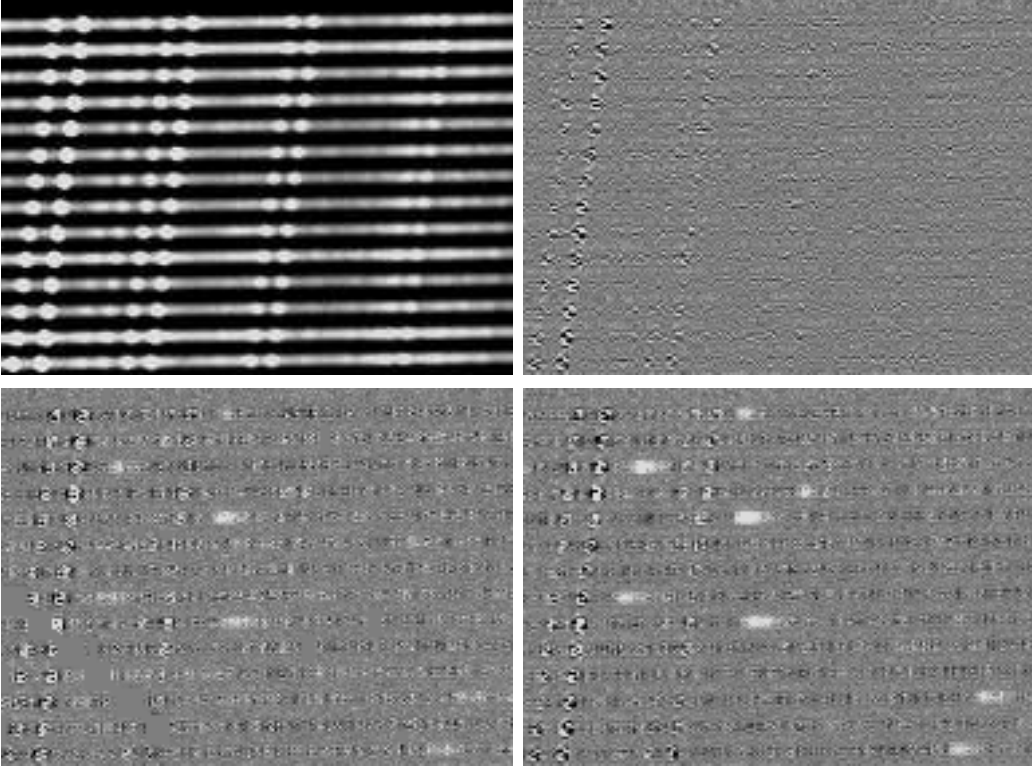


Figure 8. M2FS data reduction. Upper left panel: part of a calibrated 2D science image in SXDS3. Upper right panel: the residual of the science image after each fiber is traced, modeled, and subtracted. Lower left panel: sky-subtracted 2D image. Blank pixels are possibly affected by cosmic rays, and are not used. Lower right panel: the final combined 2D image, where we can clearly identify 7 LAEs at $z \sim 5.7$. The wavelength coverage is approximately from 8040 to 8230 Å.

ing these OH lines. This makes it particularly difficult for the detection of weak sources. Second, our targets are faint, but the spectral dispersion is high, so we take long exposures (typically one hour) for science images. This results in a number of cosmic rays and varying OH skylines. In addition, the observed OH line width is a function of spatial position in science images. This needs to be taken into account for sky subtraction.

We reduce the M2FS images using our own customized pipeline. The basic procedure is as follows. First, raw images are bias (overscan) corrected, dark subtracted, and flat-fielded. Cosmic rays are also identified and interpolated. For brevity, we call images in this step ‘calibrated’ two-dimensional (2D) images. Then we trace fiber positions using twilight images, and extract one-dimensional (1D) spectra of science, twilight, and lamp images from their calibrated 2D images. We do not use the simple box sum for spectral extraction. Instead, we fit a flux profile along the spatial direction at each pixel wavelength. The extracted 1D spectra are also used to correct small frame-to-frame positional shifts (usually 0.5 pixels per night). In Figure 8, the upper left panel shows part of a calibrated science image in SXDS3. The upper right panel shows the residual image of the science image after the above 2D profiles are subtracted.

The clean residual image suggests that the 2D profiles are well modeled. Such 2D information is used in later steps of the data reduction procedure.

Next, we perform wavelength calibration in two steps. In the first step, we derive preliminary wavelength solutions using the 1D lamp spectra. In the second step, we refine the wavelength solutions using a large number of strong OH skylines in science spectra. Then we measure fiber response curves using the 1D twilight spectra. These curves are used to correct fiber-to-fiber variations in science spectra.

Now the 1D science spectra are ready for sky subtraction. As we mentioned in Section 3.1, most of our science targets are much fainter than sky background, and their fibers can be safely used as sky fibers. As a result, more than half of all fibers are used as sky fibers. Our spectra are largely contaminated by OH skylines. The widths of OH lines vary slowly along the spatial direction in images, as illustrated in Figure 9. Therefore, a subtraction of a global sky background does not work well. The large number of sky fibers allows us to build a ‘local’ sky spectrum for each object, by averaging (with sigma rejection) flux from the nearest ~ 30 sky fibers in science images. This sky spectrum is then scaled and subtracted from the object spectrum. In order to vi-

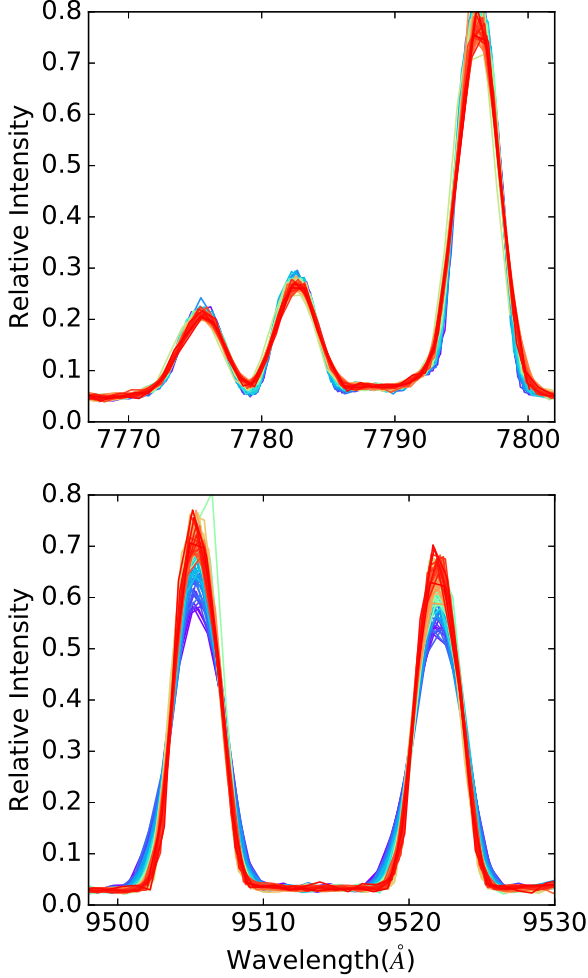


Figure 9. Variation of OH skyline width and relative intensity. The color-coded profiles represent 1D spectra extracted from all sky fibers in one SXDS3 science image. Different colors from red to blue indicates the increasing fiber numbers along the spatial direction (y-axis in the image; see Figure 8). It is clear that both line width and relative intensity of OH skylines vary slowly and smoothly along the spatial direction, which has been taken into account during our sky subtraction.

usually identify weak emission lines, we map the 1D sky spectrum of each object to a 2D sky spectrum using the 2D profile obtained when we trace fiber positions. The 2D sky spectra are then scaled and subtracted from 2D calibrated science images. The lower left panel in Figure 8 shows the sky-subtracted fibers for the same portion of the image in the other panels.

Finally, we weigh individual exposures and combine them to generate the final 1D and 2D spectra. In Figure 8, the lower right panel shows the combined 2D image. We can clearly see 7 LAEs in this portion of the image.

3.4. Preliminary Observational Results

The current depth of the observations is not uniform. The total integration time varies between 4.5 and 7.5 hrs

from field to field (Table 3). In addition, some fields were observed under relatively poor weather conditions. We are still accumulating data and improving the data reduction pipeline. On the other hand, the current stacked images are deep enough for us to securely identify relatively luminous LAEs (see the next section). Most of them are deep enough to identify $z \approx 5.7$ LAEs down to 25.5 mag.

We identify $\text{Ly}\alpha$ emission lines in our data based on both 2D images and 1D spectra (see Figures 8 and 10). Our target selection criteria usually ensure that a detected emission line in the expected wavelength range is a $\text{Ly}\alpha$ line. The main reason is that the non-detections in very deep BVR images suggest that these candidates are not likely low-redshift contaminants. We use $z \sim 5.7$ candidates as an example. The four strong emission lines in star-forming galaxies that likely contaminate our lines are $[\text{O II}] \lambda 3727$, $\text{H}\beta$, $[\text{O III}] \lambda 5007$, and $\text{H}\alpha$. The wavelength coverage rules out the possibility that a detected line is one of the $\text{H}\beta$ and $[\text{O III}] \lambda 5007$ lines, and the deep BVR images rule out the possibility that a detected line is $\text{H}\alpha$. The most likely contaminants are $[\text{O II}] \lambda 3727$ emitters. But the $[\text{O II}] \lambda 3727$ lines are doublets, and our spectral resolution is high enough to identify the doublets. A tiny fraction of the candidates are indeed confirmed to be $[\text{O II}] \lambda 3727$ emitters at lower redshift. Furthermore, we can clearly see asymmetry in the emission lines of relatively bright galaxies. This is the indicator of the $\text{Ly}\alpha$ emission line at high redshift due to strong IGM absorption blueward of the line.

We use the results from two fields, A370a and SXDS3, to demonstrate the performance of our program. These two fields are chosen for two reasons. The first reason is that the two fields have reached our designed depth. The other one is that they have the largest numbers of spectroscopically confirmed LAEs at $z \sim 5.7$ from the literature (Ouchi et al. 2005, 2008; Hu et al. 2010). There are 13 confirmed $z \sim 5.7$ LAEs in SXDS3 from Ouchi et al. (2005, 2008), and 7 confirmed $z \sim 5.7$ LAEs in A370a from Hu et al. (2010).

In A370a and SXDS3, we have 39 and 58 LAE candidates that are brighter than 7σ detections in NB816. From our data, we confirm 16 and 35 LAEs, respectively. The average detection rate is slightly above 50%, which is lower than those in the literature. This is expected. As we mentioned in Section 3.1, our target selection criteria are relatively conservative, which increases the sample completeness, but decreases the success rate. For the remaining candidates in A370a and SXDS3, there are about 10 weak emission lines that have been identified as ‘possible’ LAEs. One candidate is an $[\text{O II}] \lambda 3727$ emitter. All others are non-detections in our data.

We match our results with the LAE lists in the above literature. We find that we have recovered all 7 LAEs

in A370a from [Hu et al. \(2010\)](#), and recovered 12 out of 13 LAEs in SXDS3 from [Ouchi et al. \(2005, 2008\)](#). For the one that we do not recover, it shows a weak line that is classified as a ‘possible’ LAE in our M2FS spectra. Its emission line is also weak in the literature. Deeper spectroscopy is needed to confirm this LAE. In short, the above comparison suggests that our sample completeness is high.

4. SCIENCE GOALS AND THE FIRST RESULTS

With the M2FS survey, we will build a large sample of bright, spectroscopically confirmed LAEs and LBGs at $z \geq 6$. We are still gathering and reducing M2FS data. Based on the data processed so far and the luminosity functions from the literature, we expect to find ~ 300 $z \approx 5.7$ LAEs brighter than 25.5–25.6 mag, and ~ 60 $z \approx 6.5$ LAEs brighter than 25.1–25.2 mag. Meanwhile, we will identify a smaller sample of more than 50 fainter LAEs with high Ly α equivalent widths (their completeness will be relatively lower). In addition, we will also find a sample of bright LBGs at $z \geq 6$ and a sample of ancillary objects (Section 3.1). The unique bright LAE sample will enable much science. In this section, we will provide a few examples, such as Ly α luminosity function and its evolution, high-redshift protoclusters, physical properties of high-redshift galaxies, etc. We will also present some preliminary results, including a sample of very bright LAEs.

4.1. Science Cases

With the large sample of LAEs at $z \approx 5.7$ and 6.5, we will significantly improve the measurement of the Ly α luminosity function at these two redshifts. As we mentioned earlier, a strong evolution of the Ly α luminosity function from $z \approx 5.7$ to 6.5 has been reported, but there are large discrepancies among these results. Cosmic variance is likely one of the main reasons. The large number of galaxies over a large area will significantly reduce the uncertainty from cosmic variance. For example, assuming we find 300 LAEs at $z \approx 5.7$ in 4 deg^2 , the uncertainty from cosmic variance (including Poisson uncertainty) is only $\sim 13\%$, using the calculator of [Trenti & Stiavelli \(2008\)](#). We have assumed $\sigma_8 = 0.85$, and the average bias is ~ 7 . If we evenly split the sample into 5 luminosity bins, the uncertainty from cosmic variance for each binned luminosity function is $\sim 19\%$. In addition, our sample is well defined, with high completeness. All imaging data were taken by the same instrument (Suprime-Cam), and were reduced using the same pipeline (our own). All galaxy candidates were selected in the same way, and were spectroscopically identified by the same instrument. These factors largely reduce systematic uncertainties. With this LAE sample, we will conclusively confirm whether there is a strong evolution

of the Ly α luminosity function from $z \approx 5.7$ to 6.5. Currently, we are measuring the Ly α luminosity function at $z \approx 5.7$ based on the M2FS data taken so far ([Zheng et al.](#), in preparation).

With the bright sample of LBGs at $z \geq 6$, we will improve the measurement of the fraction of LBGs that have strong Ly α emission. This fraction is expected to decrease towards higher redshifts ($z \geq 6$), as the neutral IGM fraction becomes higher. Such a change of the fraction has been found in several LBG samples (e.g., [Stark et al. 2011](#); [Treu et al. 2012](#); [Bian et al. 2015](#)). We expect to identify a uniform LBG sample that is very suitable for calculating the fraction of LBGs with strong Ly α emission. We will measure the evolution of this fraction, which will be used to constrain the state of the IGM at these redshifts.

The LAE sample will allow us to find large protoclusters of galaxies at high redshift. In recent years, there has been growing interest in hunting for high-redshift protoclusters, the progenitors of mature clusters at low redshifts (e.g., [Ouchi et al. 2005](#); [Venemans et al. 2007](#); [Overzier et al. 2008](#); [Toshikawa et al. 2012](#); [Lee et al. 2014](#); [Dey et al. 2016](#); [Cai et al. 2017](#)). In order to reliably identify high-redshift protoclusters and measure their properties such as overdensity, spectroscopic redshifts are critical ([Chiang et al. 2013](#)). A large-area spectroscopic survey is an efficient way to find these structures. Based on the data taken so far, we have successfully identified a giant protocluster at $z \approx 5.70$ ([Jiang et al. 2017](#)). This protocluster will collapse into a galaxy cluster with a total mass significantly larger than the most massive clusters or protoclusters known at high redshift.

Our observations will enable other important science objectives, including the enhanced clustering of LAEs by patchy reionization (e.g., [McQuinn et al. 2007](#); [Jensen et al. 2014](#)) and Ly α emission halos around LAEs due to the resonant scattering of Ly α photons (e.g., [Zheng et al. 2011](#); [Jiang et al. 2013b](#); [Momose et al. 2014](#); [Lake et al. 2015](#); [Mas-Ribas & Dijkstra 2016](#); [Xue et al. 2017](#)). In addition, the deep fields that we selected are well studied with a large amount of ancillary data. In particular, these fields are (partly) covered by deep near-IR and mid-IR imaging data, such as UDS, UltraVISTA, HST CANDELS, and Spitzer Warm Mission Exploration programs. The combination of the optical and infrared data allows us to estimate a variety of physical properties of these spectroscopically confirmed galaxies, such as morphology, UV slope, star formation rate, age, dust, stellar mass, etc.

4.2. A Sample of Very Luminous LAEs

Table 4. A sample of the brightest LAEs at $z \approx 5.7$ and 6.5

No.	Field	R.A. (J2000.0)	Decl. (J2000.0)	i' (mag)	z' (mag)	NB ^a (mag)	$L(\text{Ly}\alpha)$ ($10^{43} \text{ erg s}^{-1}$)	Redshift
(1)	(2)	(3)	(4)	(5)	(6)	(7)	(8)	(9)
1	A370a	02:40:38.28	-01:30:33.0	26.28	25.82	24.28 ± 0.06	1.20 ± 0.14	5.705
2	A370a	02:39:17.66	-01:26:54.9	26.17	26.07	24.13 ± 0.05	1.74 ± 0.19	5.676
3	A370a	02:39:30.01	-01:25:29.9	26.14	26.29	24.37 ± 0.06	1.45 ± 0.17	5.676
4	A370a	02:40:08.49	-01:24:47.7	25.42	25.07	24.15 ± 0.05	1.80 ± 0.20	5.666
5	A370a	02:39:28.58	-01:24:01.4	26.26	26.62	24.24 ± 0.05	1.72 ± 0.19	5.671
6	ECDFS	03:32:15.17	-28:00:13.7	> 28.0	25.84	24.50 ± 0.08	1.88 ± 0.23	5.656
7	ECDFS	03:32:41.55	-27:59:22.3	27.78	25.75	24.45 ± 0.07	1.58 ± 0.19	5.661
8	ECDFS	03:32:37.52	-27:40:57.8	> 28.0	> 27.2	24.42 ± 0.06	1.36 ± 0.16	5.722
9	COSMOS	10:01:24.80	+02:31:45.4	> 26.9	25.82	23.72 ± 0.04	2.71 ± 0.29	6.545
10	COSMOS	09:59:54.78	+02:10:39.3	26.56	> 26.0	24.32 ± 0.02	1.89 ± 0.19	5.664
11	SXDS1	02:17:57.60	-05:08:44.9	> 27.9	25.67	23.56 ± 0.05	4.78 ± 0.53	6.595
12	SXDS1	02:19:01.44	-04:58:59.0	> 27.9	> 26.8	24.43 ± 0.06	1.54 ± 0.27	6.556
13	SXDS1	02:18:27.45	-04:47:37.2	26.33	25.93	23.87 ± 0.04	1.96 ± 0.21	5.703
14	SXDS2	02:18:06.23	-04:45:10.8	> 27.9	26.71	24.16 ± 0.06	2.24 ± 0.26	6.577
15	SXDS2	02:18:29.02	-04:35:08.1	27.47	25.52	24.12 ± 0.06	1.96 ± 0.22	6.513
16	SXDS2	02:17:34.58	-04:45:59.1	26.62	25.64	24.45 ± 0.06	1.03 ± 0.12	5.702
17	SXDS2	02:18:23.30	-04:43:35.1	26.11	25.05	24.50 ± 0.06	1.05 ± 0.12	5.670
18	SXDS2	02:17:58.92	-04:30:30.5	26.63	25.98	24.26 ± 0.05	1.30 ± 0.14	5.690
19	SXDS3	02:17:14.01	-05:36:48.8	26.29	24.69	23.55 ± 0.04	2.07 ± 0.22	6.530
20	SXDS3	02:17:29.49	-05:38:16.6	26.21	26.05	24.35 ± 0.07	1.53 ± 0.18	5.671
21	SXDS3	02:17:52.65	-05:35:11.8	25.11	24.57	24.05 ± 0.04	3.20 ± 0.34	5.759
22	SXDS3	02:17:07.87	-05:34:26.8	26.39	26.04	23.61 ± 0.03	2.75 ± 0.29	5.680
23	SXDS3	02:17:24.04	-05:33:09.7	25.68	25.05	23.48 ± 0.02	2.70 ± 0.27	5.708
24	SXDS3	02:17:48.47	-05:31:27.1	26.30	25.64	24.26 ± 0.05	1.24 ± 0.14	5.690
25	SXDS3	02:17:45.26	-05:29:36.1	26.55	25.97	24.03 ± 0.04	1.76 ± 0.19	5.688
26	SXDS3	02:17:49.13	-05:28:54.3	26.08	25.60	24.04 ± 0.04	1.62 ± 0.17	5.696
27	SXDS3	02:17:04.30	-05:27:14.4	26.30	26.25	23.98 ± 0.04	1.89 ± 0.20	5.687
28	SXDS3	02:17:36.39	-05:27:01.8	26.89	> 26.8	24.48 ± 0.06	1.33 ± 0.15	5.674
29	SXDS3	02:16:57.89	-05:21:17.1	26.69	> 26.8	24.46 ± 0.06	1.55 ± 0.18	5.669
30	SXDS5	02:16:05.11	-05:07:54.0	26.16	25.23	24.29 ± 0.06	1.88 ± 0.21	5.654
31	SXDS5	02:15:25.26	-04:59:18.3	26.63	25.70	24.24 ± 0.06	1.35 ± 0.15	5.674
32	SXDS5	02:16:24.72	-04:55:16.7	26.41	25.92	23.71 ± 0.04	1.91 ± 0.20	5.707

^aNB indicates NB816 for $z \approx 5.7$ LAEs, and NB921 (or NB912) for $z \approx 6.5$ LAEs.

Recently, the most luminous LAEs at $z \geq 6$, such as ‘Himiko’, ‘Masosa’, ‘CR7’, and ‘COLA1’, have received much attention (e.g., [Ouchi et al. 2009](#); [Lidman et al. 2012](#); [Sobral et al. 2015](#); [Zabl et al. 2015](#); [Hu et al. 2016](#)). For example, ‘CR7’ has been suggested to harbor a direct-collapse black hole, a massive seed of a supermassive black hole (e.g., [Dijkstra et al. 2016](#);

[Latif & Ferrara 2016](#)). It has also been suggested that ‘CR7’ contains Population III-like stars (e.g., [Pallottini et al. 2015](#); [Sobral et al. 2015](#)), though the claim is still controversial (e.g., [Bowler et al. 2017b](#)). Nevertheless, these extreme objects may have played important roles in the early massive black hole formation, Population III stellar populations, and cosmic reioniza-

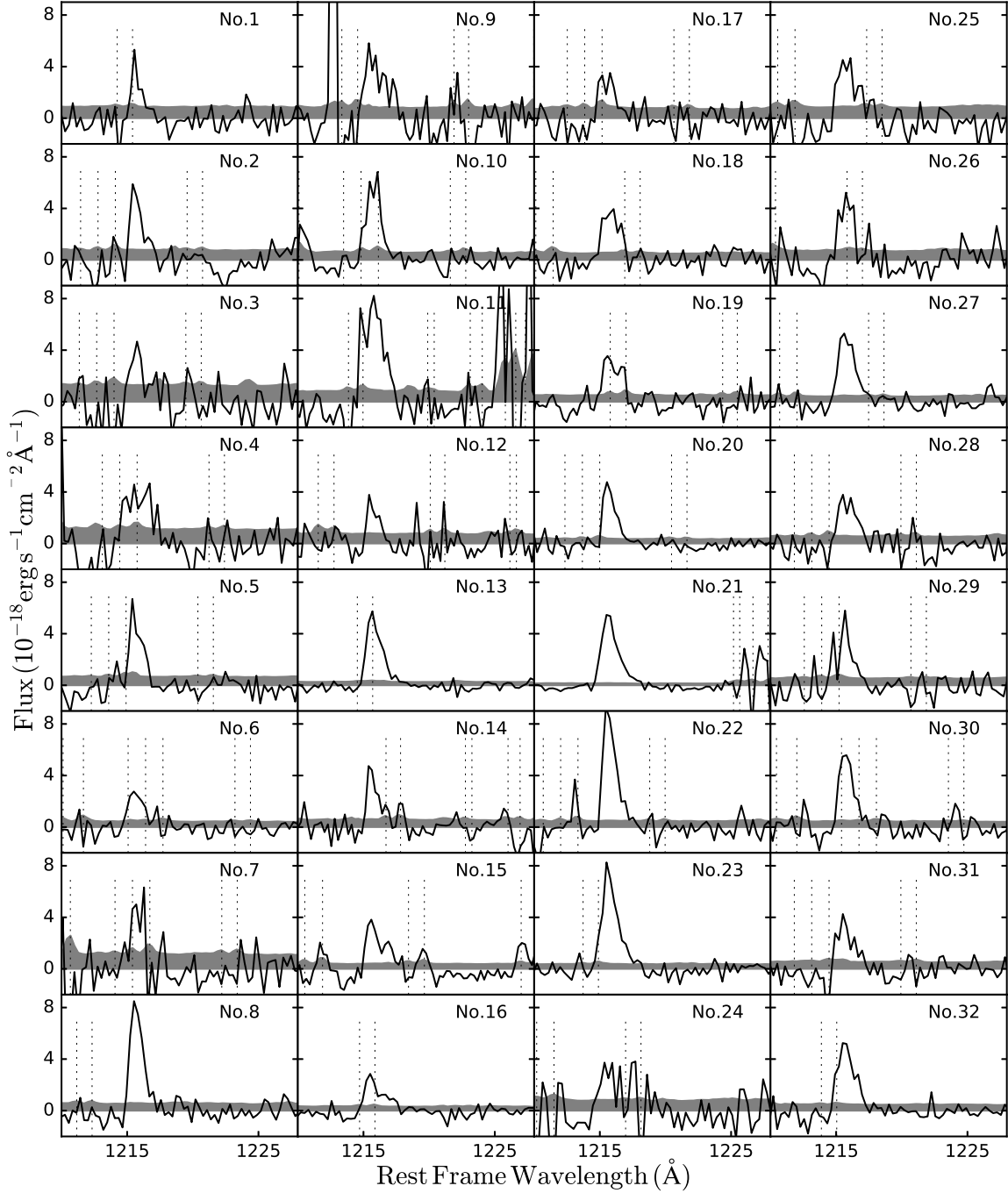


Figure 10. M2FS spectra of the 32 luminous LAEs. The spectra have been scaled to match the observed narrow-band photometry in Table 4. For each LAE, the gray region indicates the 1σ uncertainty region, and the bottom of the gray region indicates the zero-flux level. The vertical dotted lines show the positions of OH skylines. The object number corresponds to the number in Column 1 of Table 4.

tion.

In this subsection, we present a sample of very luminous LAEs at $z \approx 5.7$ and 6.5 . As we mentioned earlier, the current depths of the M2FS data are not uniform across the fields. The LAE sample presented here is from part of the data that have been fully processed. The LAEs are selected to have narrow-band magnitudes

brighter than 24.5 mag, roughly corresponding to a $\text{Ly}\alpha$ luminosity of $L \sim 10^{43} \text{ erg s}^{-1}$. This is about half of the ‘CR7’ $\text{Ly}\alpha$ luminosity. Some LAEs in this sample are even brighter than ‘CR7’.

The sample of 32 luminous LAEs are summarized in Table 4. Columns 3 and 4 give the coordinates of the LAEs. Columns 5 through 7 show their i' , z' , and

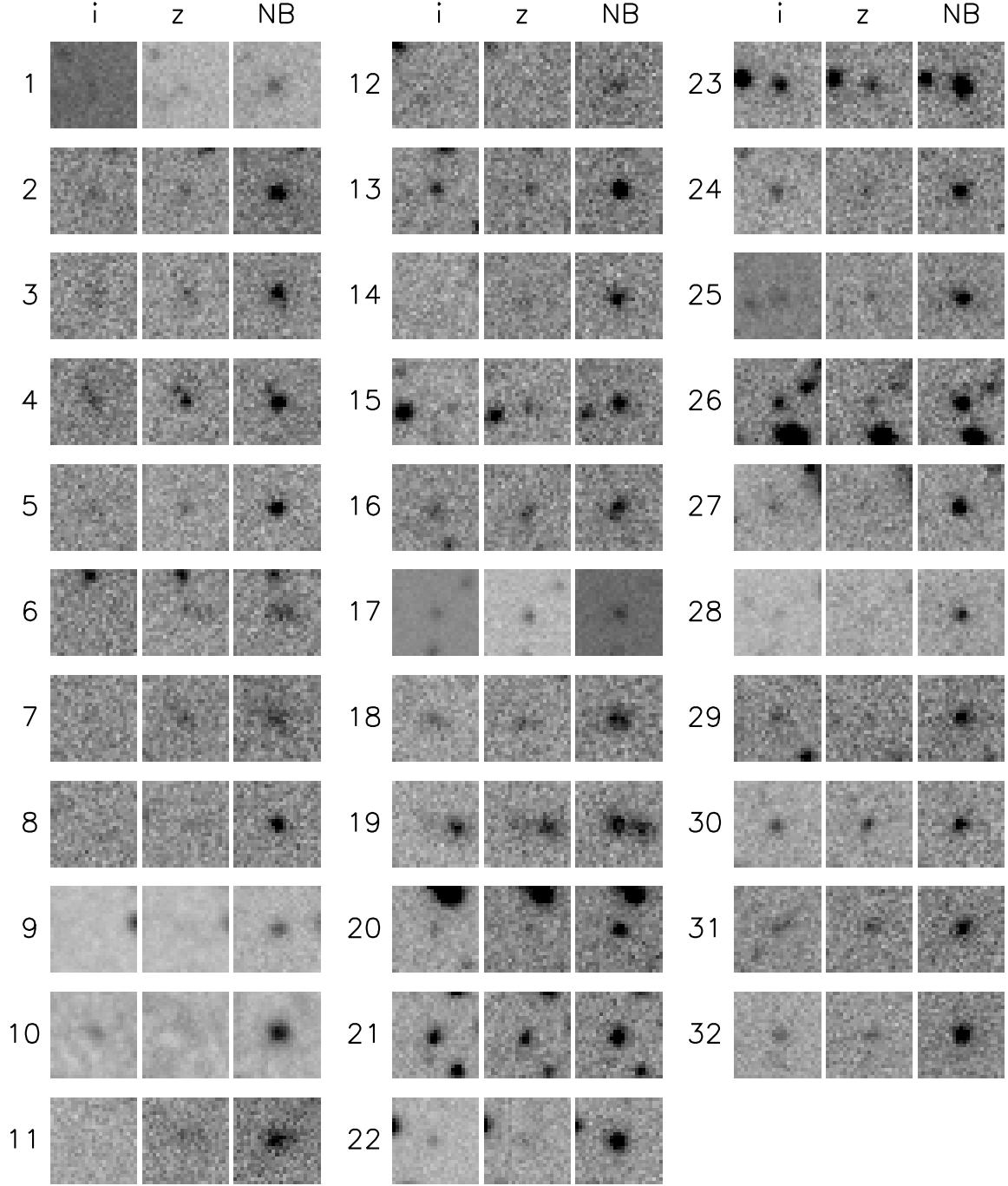


Figure 11. Thumbnail images of the 32 luminous LAEs in the i' , z' , and narrow bands. The image size is 25×25 pixels, or $5'' \times 5''$. The objects numbers correspond to the numbers shown in Column 1 in Table 4. NB indicates NB816 for $z \approx 5.7$ LAEs and NB921 (or NB912) for $z \approx 6.5$ LAEs. They represent the most luminous LAEs at $z \geq 6$.

narrow-band photometry. Column 8 shows the $\text{Ly}\alpha$ luminosities. Column 9 shows the redshifts measured from their $\text{Ly}\alpha$ emission lines. These LAEs are among the brightest of all known LAEs at $z \geq 6$. In particular, about 25% of them are brighter than 24 mag, and they are comparable to ‘CR7’ in terms of $\text{Ly}\alpha$ luminosity. A few of them reach $\text{NB} \approx 23.5$ mag, as bright as the most luminous LAE known, ‘COLA1’. Note that our obser-

vations did not cover ‘CR7’ and ‘COLA1’, but covered ‘Himiko’ (No. 11 in Table 4) and ‘Masosa’ (No. 9). The first 5 LAEs in Table 4 are from the A370a field, but none of them was reported by [Hu et al. \(2010\)](#), for unknown reasons.

Figure 10 shows the M2FS spectra of the 32 LAEs. Figure 11 shows the thumbnail images of the 32 LAEs in the i' , z' , and one of the narrow bands (NB816 for

$z \approx 5.7$ LAEs, and NB921 or NB912 for $z \approx 6.5$ LAEs). The brightest galaxies at $z \geq 6$ generally display extended features or multiple clumps in deep *HST* images (e.g. Jiang et al. 2013b). These features are not so obvious in ground-based images. Owing to the excellent image quality ($0.6'' - 0.8''$), however, most LAEs in Figure 11 clearly show extended (or diffuse) Ly α emission. A detailed structural and morphological study of these LAEs will be presented in a following paper (Bian et al., in preparation).

5. SUMMARY

We have presented an overview of our ongoing program aimed to build a large and homogeneous sample of luminous LAEs at $z \approx 5.7$ and 6.5 , and LBGs at $5.5 < z < 6.8$. The fields that we chose to observe are well-studied, including SXDS, A370, ECDFS, COSMOS, and SSA22. They cover a total of nearly 4 square degrees on the sky. These fields have deep optical imaging data in a series of broad and narrow bands, taken by the prime-focus imager Suprime-Cam on the 8.2-m Subaru telescope. The multi-band data have allowed us to efficiently select galaxy candidates via the narrow-band (or Ly α) and Lyman-break techniques. In particular, we have used two narrow-band images, NB816 and NB921 (or NB912), to select candidate LAEs at $z \approx 5.7$ and 6.5 .

We are carrying out spectroscopic observations to identify these galaxy candidates, using the fiber-fed, multi-object spectrograph M2FS on the 6.5-m Magellan Clay telescope. M2FS has 256 optical fibers deployed over a large circular FoV $\sim 30'$ in diameter, making it one of the most efficient instruments to identify distant galaxies. With a total of 5–6 hour on-source integration per pointing, we are able to identify $z \approx 5.7$ LAEs down to at least NB816 $\approx 25.5 - 25.6$ mag, corresponding to a Ly α flux depth of $\sim 1 \times 10^{-17}$ erg s $^{-1}$ cm $^{-2}$, or a luminosity depth of $\sim 4 \times 10^{42}$ erg s $^{-1}$. We have observed ~ 2.5 square degrees so far. When the program is completed, we expect to find more than 300 $z \approx 5.7$ LAEs brighter than NB816 = 25.5 mag, more than 60 $z \approx 6.5$ LAEs brighter than NB921 = 25.2 mag, a smaller sample of fainter LAEs, and a substantial number of bright LBGs at $z \geq 6$. We will also identify a large sample of ancillary objects at lower redshift.

We have outlined some of our science goals, including

investigation of Ly α luminosity function and its evolution, large protoclusters, and cosmic reionization. Particularly, the large LAE sample over a large area will allow us to obtain an accurate Ly α luminosity function and answer an important question: whether there is a strong evolution between $z \approx 5.7$ and 6.5 . Our fields are partly covered by rich ancillary data in multiple wavebands, which will be used to study a variety of physical properties of high-redshift galaxies. We have also presented one of the first results: a sample of very luminous LAEs at $z \approx 5.7$ and 6.5 . This sample consists of 32 LAEs brighter than 24.5 mag (in the narrow bands). Some of them are as bright as the two most luminous LAEs known at $z \geq 6$, ‘CR7’ and ‘COLA1’. Thus, this sample represents the brightest LAEs at $z \geq 6$.

Currently we are still accumulating data for this program and improving the data reduction pipeline. We expect to complete all M2FS observations in one year.

We acknowledge support from National Key Program for Science and Technology Research and Development (grants 2016YFA0400702 and 2016YFA0400703), and from the National Science Foundation of China (grant 11533001). YS acknowledges support from an Alfred P. Sloan Research Fellowship. This work is accomplished (in part) with the support from the Chinese Academy of Sciences (CAS) through a China-Chile Joint Research Fund (CCJRF) #1503 administered by the CAS South America Center for Astronomy (CASSACA) in Santiago, Chile. This paper includes data gathered with the 6.5 meter Magellan Telescopes located at Las Campanas Observatory, Chile. Australian access to the Magellan Telescopes was supported through the National Collaborative Research Infrastructure Strategy of the Australian Federal Government. This research uses data obtained through the Telescope Access Program (TAP), which has been funded by the National Astronomical Observatories of China (the Strategic Priority Research Program “The Emergence of Cosmological Structures” Grant No. XDB09000000), and the Special Fund for Astronomy from the Ministry of Finance. This work is based in part on data collected at Subaru Telescope and obtained from the SMOKA, which is operated by the Astronomy Data Center, National Astronomical Observatory of Japan.

Facilities: Magellan:Clay (M2FS)

REFERENCES

- Baba, H., Yasuda, N., Ichikawa, S.-I., et al. 2002, *Astronomical Data Analysis Software and Systems XI*, 281, 298
- Bagley, M. B., Scarlata, C., Henry, A., et al. 2017, *ApJ*, 837, 11
- Bertin, E. 2006, *Astronomical Data Analysis Software and Systems XV*, 351, 112
- Bertin, E., & Arnouts, S. 1996, *A&AS*, 117, 393
- Bertin, E., Mellier, Y., Radovich, M., et al. 2002, *Astronomical Data Analysis Software and Systems XI*, 281, 228
- Bian, F., Stark, D. P., Fan, X., et al. 2015, *ApJ*, 806, 108

- Bouwens, R. J., Illingworth, G. D., Oesch, P. A., et al. 2014, *ApJ*, 793, 115
- Bouwens, R. J., Bradley, L., Zitrin, A., et al. 2014, *ApJ*, 795, 126
- Bouwens, R. J., Illingworth, G. D., Oesch, P. A., et al. 2015, *ApJ*, 803, 34
- Bowler, R. A. A., Dunlop, J. S., McLure, R. J., et al. 2012, *MNRAS*, 426, 2772
- Bowler, R. A. A., Dunlop, J. S., McLure, R. J., & McLeod, D. J. 2017, *MNRAS*, 466, 3612
- Bowler, R. A. A., McLure, R. J., Dunlop, J. S., et al. 2017, *MNRAS*, 469, 448
- Cai, Z.-Y., Lapi, A., Bressan, A., et al. 2014, *ApJ*, 785, 65
- Cai, Z., Fan, X., Bian, F., et al. 2017, *ApJ*, 839, 131
- Capak, P., Aussel, H., Ajiki, M., et al. 2007, *ApJS*, 172, 99
- Castellano, M., Pentericci, L., Fontana, A., et al. 2017, *ApJ*, 839, 73
- Chiang, Y.-K., Overzier, R., & Gebhardt, K. 2013, *ApJ*, 779, 127
- Coe, D., Zitrin, A., Carrasco, M., et al. 2013, *ApJ*, 762, 32
- Curtis-Lake, E., McLure, R. J., Dunlop, J. S., et al. 2016, *MNRAS*, 457, 440
- Curtis-Lake, E., McLure, R. J., Pearce, H. J., et al. 2012, *MNRAS*, 422, 1425
- Dey, A., Lee, K.-S., Reddy, N., et al. 2016, *ApJ*, 823, 11
- Dijkstra, M. 2014, *PASP*, 31, 40
- Dijkstra, M., Gronke, M., & Sobral, D. 2016, *ApJ*, 823, 74
- Dressler, A., Martin, C. L., Henry, A., Sawicki, M., & McCarthy, P. 2011, *ApJ*, 740, 71
- Dunlop, J. S., McLure, R. J., Robertson, B. E., et al. 2012, *MNRAS*, 420, 901
- Egami, E., Kneib, J.-P., Rieke, G. H., et al. 2005, *ApJL*, 618, L5
- Ellis, R. S., McLure, R. J., Dunlop, J. S., et al. 2013, *ApJL*, 763, L7
- Faisst, A. L., Capak, P., Hsieh, B. C., et al. 2016, *ApJ*, 821, 122
- Fan, X., Carilli, C. L., & Keating, B. 2006, *ARA&A*, 44, 415
- Finkelstein, S. L., Papovich, C., Dickinson, M., et al. 2013, *Nature*, 502, 524
- Finkelstein, S. L., Papovich, C., Salmon, B., et al. 2012, *ApJ*, 756, 164
- Furusawa, H., Kosugi, G., Akiyama, M., et al. 2008, *ApJS*, 176, 1
- González, V., Bouwens, R., Illingworth, G., et al. 2014, *ApJ*, 781, 34
- Grogin, N. A., Kocevski, D. D., Faber, S. M., et al. 2011, *ApJS*, 197, 35
- Guaita, L., Melinder, J., Hayes, M., et al. 2015, *A&A*, 576, A51
- Harikane, Y., Ouchi, M., Ono, Y., et al. 2017, *arXiv:1704.06535*
- Henry, A. L., Martin, C. L., Dressler, A., Sawicki, M., & McCarthy, P. 2012, *ApJ*, 744, 149
- Hibon, P., et al. 2010, *A&A*, 515, 97
- Hu, E. M., Cowie, L. L., Barger, A. J., et al. 2010, *ApJ*, 725, 394
- Hu, E. M., Cowie, L. L., McMahon, R. G., et al. 2002, *ApJL*, 568, L75
- Hu, E. M., Cowie, L. L., Songaila, A., et al. 2016, *ApJL*, 825, L7
- Infante, L., Zheng, W., Laporte, N., et al. 2015, *ApJ*, 815, 18
- Iye, M., Ota, K., Kashikawa, N., et al. 2006, *Nature*, 443, 186
- Jensen, H., Hayes, M., Iliev, I. T., et al. 2014, *MNRAS*, 444, 2114
- Jiang, L., Egami, E., Fan, X., et al. 2013, *ApJ*, 773, 153
- Jiang, L., Egami, E., Kashikawa, N., et al. 2011, *ApJ*, 743, 65
- Jiang, L., Egami, E., Mechtley, M., et al. 2013, *ApJ*, 772, 99
- Jiang, L., Finlator, K., Cohen, S. H., et al. 2016, *ApJ*, 816, 16
- Jiang, L., Wu, J., Bian, F., et al. 2017, submitted
- Kakiichi, K., Dijkstra, M., Ciardi, B., & Graziani, L. 2016, *MNRAS*, 463, 4019
- Karman, W., Caputi, K. I., Caminha, G. B., et al. 2017, *A&A*, 599, A28
- Kashikawa, N., Shimasaku, K., Malkan, M. A., et al. 2006, *ApJ*, 648, 7
- Kashikawa, N., Shimasaku, K., Matsuda, Y., et al. 2011, *ApJ*, 734, 119
- Kashikawa, N., Shimasaku, K., Yasuda, N., et al. 2004, *PASJ*, 56, 1011
- Kawamata, R., Ishigaki, M., Shimasaku, K., Oguri, M., & Ouchi, M. 2015, *ApJ*, 804, 103
- Kobayashi, M. A. R., Murata, K. L., Koekemoer, A. M., et al. 2016, *ApJ*, 819, 25
- Kodaira, K., Taniguchi, Y., Kashikawa, N., et al. 2003, *PASJ*, 55, L17
- Koekemoer, A. M., Faber, S. M., Ferguson, H. C., et al. 2011, *ApJS*, 197, 36
- Konno, A., Ouchi, M., Ono, Y., et al. 2014, *ApJ*, 797, 16
- Konno, A., Ouchi, M., Shibuya, T., et al. 2017, *arXiv:1705.01222*
- Krug, H. B., Veilleux, S., Tilvi, V., et al. 2012, *ApJ*, 745, 122
- Lake, E., Zheng, Z., Cen, R., et al. 2015, *ApJ*, 806, 46
- Laporte, N., Pelló, R., Hayes, M., et al. 2012, *A&A*, 542, L31
- Laporte, N., Streblyanska, A., Kim, S., et al. 2015, *A&A*, 575, AA92
- Latif, M. A., & Ferrara, A. 2016, *PASA*, 33, e051
- Lee, K.-S., Dey, A., Hong, S., et al. 2014, *ApJ*, 796, 126
- Lehmer, B. D., Brandt, W. N., Alexander, D. M., et al. 2005, *ApJS*, 161, 21
- Lidman, C., Hayes, M., Jones, D. H., et al. 2012, *MNRAS*, 420, 1946
- Liu, C., Mutch, S. J., Poole, G. B., et al. 2017, *MNRAS*, 465, 3134
- Lotz, J. M., Koekemoer, A., Coe, D., et al. 2017, *ApJ*, 837, 97
- Luo, B., Brandt, W. N., Xue, Y. Q., et al. 2017, *ApJS*, 228, 2
- Mas-Ribas, L., & Dijkstra, M. 2016, *ApJ*, 822, 84
- Mateo, M., Bailey, J. I., Crane, J., et al. 2012, *Proc. SPIE*, 8446, 84464Y
- Matthee, J., Sobral, D., Santos, S., et al. 2015, *MNRAS*, 451, 400
- McLeod, D. J., McLure, R. J., & Dunlop, J. S. 2016, *MNRAS*, 459, 3812
- McQuinn, M., Hernquist, L., Zaldarriaga, M., & Dutta, S. 2007, *MNRAS*, 381, 75
- Miyazaki, S., Komiyama, Y., Sekiguchi, M., et al. 2002, *PASJ*, 54, 833
- Momose, R., Ouchi, M., Nakajima, K., et al. 2014, *MNRAS*, 442, 110
- Murayama, T., Taniguchi, Y., Scoville, N. Z., et al. 2007, *ApJS*, 172, 523
- Oesch, P. A., Bouwens, R. J., Illingworth, G. D., et al. 2014, *ApJ*, 786, 108
- Oesch, P. A., Brammer, G., van Dokkum, P. G., et al. 2016, *ApJ*, 819, 129
- Oesch, P. A., van Dokkum, P. G., Illingworth, G. D., et al. 2015, *ApJL*, 804, L30
- Ono, Y., Ouchi, M., Harikane, Y., et al. 2017, *arXiv:1704.06004*
- Ota, K., & Iye, M. 2012, *MNRAS*, 423, 444
- Ota, K., Iye, M., Kashikawa, N., et al. 2017, *arXiv:1703.02501*
- Ouchi, M., Shimasaku, K., Akiyama, M., et al. 2005, *ApJL*, 620, L1
- Ouchi, M., Shimasaku, K., Akiyama, M., et al. 2008, *ApJS*, 176, 301
- Ouchi, M., Ono, Y., Egami, E., et al. 2009, *ApJ*, 696, 1164
- Ouchi, M., Shimasaku, K., Furusawa, H., et al. 2010, *ApJ*, 723, 869
- Ouchi, M., Harikane, Y., Shibuya, T., et al. 2017, *ApJ*, 843, 133
- Overzier, R. A., Bouwens, R. J., Cross, N. J. G., et al. 2008, *ApJ*, 673, 143-162
- Oyarzún, G. A., Blanc, G. A., González, V., et al. 2016, *ApJL*, 821, L14
- Oyarzún, G. A., Blanc, G. A., González, V., Mateo, M., & Bailey, J. I., III 2017, *arXiv:1706.01886*
- Pallottini, A., Ferrara, A., Pacucci, F., et al. 2015, *MNRAS*, 453, 2465

- Pentericci, L., Carniani, S., Castellano, M., et al. 2016, *ApJL*, 829, L11
- Rhoads, J. E., Hibon, P., Malhotra, S., Cooper, M., & Weiner, B. 2012, *ApJL*, 752, L28
- Rhoads, J. E., Xu, C., Dawson, S., et al. 2004, *ApJ*, 611, 59
- Roberts-Borsani, G. W., Bouwens, R. J., Oesch, P. A., et al. 2016, *ApJ*, 823, 143
- Planck Collaboration, Adam, R., Aghanim, N., et al. 2016, *arXiv:1605.03507*
- Santos, S., Sobral, D., & Matthee, J. 2016, *MNRAS*, 463, 1678
- Schmidt, K. B., Treu, T., Bradač, M., et al. 2016, *ApJ*, 818, 38
- Scoville, N., Aussel, H., Brusa, M., et al. 2007, *ApJS*, 172, 1
- Shimasaku, K., Kashikawa, N., Doi, M., et al. 2006, *PASJ*, 58, 313
- Shibuya, T., Kashikawa, N., Ota, K., et al. 2012, *ApJ*, 752, 114
- Shibuya, T., Ouchi, M., & Harikane, Y. 2015, *ApJS*, 219, 15
- Shibuya, T., Ouchi, M., Kubo, M., & Harikane, Y. 2016, *ApJ*, 821, 72
- Shibuya, T., Ouchi, M., Konno, A., et al. 2017, *arXiv:1704.08140*
- Silva, M. B., Santos, M. G., Gong, Y., Cooray, A., & Bock, J. 2013, *ApJ*, 763, 132
- Sobral, D., Matthee, J., Darvish, B., et al. 2015, *ApJ*, 808, 139
- Song, M., Finkelstein, S. L., Livermore, R. C., et al. 2016, *ApJ*, 826, 113
- Stark, D. P., Ellis, R. S., & Ouchi, M. 2011, *ApJL*, 728, L2
- Stark, D. P., Schenker, M. A., Ellis, R. S., et al. 2013, *ApJ*, 763, 129
- Taniguchi, Y., Ajiki, M., Nagao, T., et al. 2005, *PASJ*, 57, 165
- Taniguchi, Y., Scoville, N., Murayama, T., et al. 2007, *ApJS*, 172, 9
- Tilvi, V., Pirzkal, N., Malhotra, S., et al. 2016, *ApJL*, 827, L14
- Tilvi, V., Rhoads, J. E., Hibon, P., et al. 2010, *ApJ*, 721, 1853
- Toshikawa, J., Kashikawa, N., Ota, K., et al. 2012, *ApJ*, 750, 137
- Trenti, M., & Stiavelli, M. 2008, *ApJ*, 676, 767
- Treu, T., Schmidt, K. B., Trenti, M., Bradley, L. D., & Stiavelli, M. 2013, *ApJL*, 775, 29
- Treu, T., Trenti, M., Stiavelli, M., Auger, M. W., & Bradley, L. D. 2012, *ApJ*, 747, 27
- Venemans, B. P., Röttgering, H. J. A., Miley, G. K., et al. 2007, *A&A*, 461, 823
- Watson, D., Christensen, L., Knudsen, K. K., et al. 2015, *Nature*, 519, 327
- Willott, C. J., McLure, R. J., Hibon, P., et al. 2013, *AJ*, 145, 4
- Xue, R., Lee, K.-S., Dey, A., et al. 2017, *ApJ*, 837, 172
- Xue, Y. Q., Luo, B., Brandt, W. N., et al. 2016, *ApJS*, 224, 15
- Yagi, M., Kashikawa, N., Sekiguchi, M., et al. 2002, *AJ*, 123, 66
- Yagi, M. S., Nao, Yamanoi, H., Furusawa, H., Nakata, F., & Komiyama, Y. 2013, *PASJ*, 65, 22
- Yan, H., Finkelstein, S. L., Huang, K.-H., et al. 2012, *ApJ*, 761, 177
- Zabl, J., Nørgaard-Nielsen, H. U., Fynbo, J. P. U., et al. 2015, *MNRAS*, 451, 2050
- Zheng, Z., Cen, R., Weinberg, D., Trac, H., & Miralda-Escudé, J. 2011, *ApJ*, 739, 62
- Zheng, Z.-Y., Wang, J., Rhoads, J., et al. 2017, *ApJL*, 842, L22
- Zitrin, A., Ellis, R. S., Belli, S., & Stark, D. P. 2015, *ApJL*, 805, L7